Measurement of Ionospheric Faraday Rotation in Simulated and Real Spaceborne SAR Data

Michael Jehle, *Student Member, IEEE*, Maurice Rüegg, *Member, IEEE*, Lukas Zuberbühler, David Small, *Member, IEEE*, and Erich Meier

***Abstract*—The influence of the atmosphere on a frequency-modulated electromagnetic wave traversing the ionosphere is becoming increasingly important for recent and upcoming low-frequency and wide-bandwidth spaceborne synthetic aperture radar (SAR) systems. The ionized ionosphere induces Faraday rotation (FR) at these frequencies that affects radar polarimetry and causes signal path delays resulting in a reduced range resolution. The work at hand introduces a simulation model of SAR signals passing through the atmosphere, including both frequency-dependent FR and path delays. Based on simulation results from this model [proven with real Advanced Land Observing Satellite Phased Array L-band Synthetic Aperture Radar (PALSAR) data], estimation of FR in quad-polarized SAR data using the given approach is shown for raw, range-compressed, and focused radar images. Path delays and signal chirp bandwidth effects are considered. Investigations discuss the suitability of raw and compressed data versus combination of total electron content maps with the Earth's magnetic field for FR estimation and deduced from a large number of analyzed PALSAR data sets.**

***Index Terms*—Advanced Land Observing Satellite (ALOS) Phased Array L-band Synthetic Aperture Radar (PALSAR), Faraday rotation (FR), ionosphere, SAR processing, synthetic aperture radar (SAR), total electron content (TEC).**

I. Introduction

With the successful launch of the Advanced Land Observing Satellite (ALOS) and the on-board Phased Array L-band Synthetic Aperture Radar (PALSAR) instrument, spaceborne synthetic aperture radar (SAR) data at L-band have become available with a relatively wide bandwidth. Depending on the acquisition mode, the sensor's range chirp bandwidth can be as high as 28 MHz. However, in high solar conditions, ionospheric path delays and Faraday rotation (FR) become significant for wide-bandwidth SAR applications [1]; the use of large chirp bandwidths is susceptible to signal degradation that can result in a suboptimal resolution, and FR may distort or even destroy important information otherwise available from polarimetric SAR data.

A preliminary study was directed toward how the influence of the ionosphere on SAR becomes significant at low frequencies starting at L-band and lower and how signal degradation caused by the ionized ionosphere increases with larger chirp bandwidths [2], [3]. The aim here is the development and description of algorithms and system models estimating ionospheric FR of electromagnetic waves from quad-polarized SAR data. Raw or focused radar images can be used for the estimation. Based on simulations and proven with real PALSAR data, the algorithms are based on known techniques for ionospheric total electron content (TEC) measurements. The electron content is responsible for FR [1]. Additional influences of ionospheric TEC such as path delays and signal reception degradation are considered for the simulations and discussed also in the real data. Once FR and TEC are known, fully polarimetric data sets can be calibrated and used for polarimetric SAR analyses. Resolution degradations may also be corrected.

The potential of low-frequency SAR with ionospheric path delays and FR for TEC measurements has been recognized in [2] and [4]. FR effects have been discussed at length in [1], [5], and [6]. Corrective methods were treated, e.g., in [7]. Distortion effects are laid out in [8]–[10]. Detection and estimation techniques based on quad-polarized data are presented in [1], [11], and [12]. A good estimation aids and improves general polarimetric calibration and validation techniques, such as given in [13] and [14], to make spaceborne polarimetric measurements trustworthy for biomass classification and retrieval [15], [16]. In [17], the first analysis of PALSAR data considering FR detection is presented.

In Section II, the theoretical background of the ionospheric influences on electromagnetic waves is outlined. Section III introduces the algorithms used for the simulation of spaceborne SAR data of a point target, including quad-polarization and FR. The influence of frequency-dependent radar chirp path delays is explained and added to the simulation. The simulations are carried out for typical L- and P-band sensor configurations. For the estimation of FR, the approach of frequency-dependent rotation of a linearly polarized wave is applied. The simulations are based on point targets, exploiting the information from quad-polarized data, and are performed using techniques proposed in [1]. Investigations discuss the suitability of raw, range-compressed (RC), and azimuth-compressed (AC) data for FR estimation. Empirical results obtained from PALSAR scenes are shown in Section IV together with the calibration steps necessary to acquire them correctly. Simulated and real data are compared and discussed in Section V. Possible methods for properly validating the approaches are suggested. A conclusion with a summary of results, possible improvements, and directions for further research is given in Section VI.

Manuscript received December 21, 2007; revised March 14, 2008, and May 28, 2008. First published December 2, 2008; current version published April 24, 2009. This work was supported by the European Space Agency (ESA) under Contract 20046/06/NL/CO.

M. Jehle, L. Zuberbühler, D. Small, and E. Meier are with the Remote Sensing Laboratories, University of Zürich, 8057 Zürich, Switzerland (e-mail: michael.jehle@geo.uzh.ch).

M. Rüegg is with the UBS Investment Bank, 8152 Opfikon, Switzerland.

Digital Object Identifier 10.1109/TGRS.2008.2004710

II. Effects of the Ionosphere

Electromagnetic waves propagating through the ionosphere experience a polarization rotation of the electric field vector and a signal path delay that depends on the number of free electrons N_e along the ray path, the signal frequency f, and the strength of the magnetic field parallel to the propagation direction of the wave within the ionized layer. Entering an ionized medium, a linearly polarized wave can be regarded as a superposition of two separate counter-rotating circular polarized waves, traveling on slightly different paths with different velocities. Leaving the ionized medium, these waves recombine with a resulting polarization that is dependent on these propagating effects. The two-way propagation from a satellite to the Earth and back does *not* compensate for this effect. The effect is cumulative: FR *doubles*, as does the path delay [18].

A. Earth Magnetic Field and Free Electrons in the Ionosphere

A widely used model for the estimation of the geomagnetic field of the Earth is the International Geomagnetic Reference Field (IGRF) model. The latest version is the tenth generation of the model and was released by the International Association of Geomagnetism and Aeronomy [19]. It is described mathematically by a series of spherical harmonics, the coefficients of which are estimated on the order of 13. The main field can be approximated as a dipole centered within the Earth and caused by electric currents within the Earth. The magnetic field is therefore modeled as the negative gradient of the potential V and can be written as [19]

$$V(r,\theta,\psi,t) = R\sum_{n=1}^{n_{\max}}\left(\frac{R}{r}\right)^{n+1}\sum_{m=0}^{n}\left(g_n^m(t)\cos(m\psi)+h_n^m(t)\cdot\sin(m\psi)\right)P_n^m(\theta) \quad (1)$$

where r is the distance from the center of the Earth, θ is the co-latitude (i.e., 90° latitude), ψ is the longitude, R is the reference radius of the Earth, $g_n^m(t)$ and $h_n^m(t)$ are the field coefficients at time t, and $P_n^m(\theta)$ are the Schmidt seminormalized associated Legendre functions of degree n and order m.

The model's coefficients of the spherical harmonic vary in time. Their period of validity is normally set to five years. More details on main-field modeling can be found in [20] and [21]. Fig. 1 shows a plot of the nadir component relative to the Earth's center of the global magnetic field as modeled by the IGRF10 for June 21, 2007.

B. FR

The polarization rotation of the E-field vector of an electromagnetic wave traveling through the ionosphere is called FR as mentioned in the introduction. It depends on the total electron content along the ray path, its wavelength, and the Earth's magnetic field. In Fig. 1, it may be seen that there is no FR at the geomagnetic equator for a nadir-looking sensor configuration. If the geomagnetic field is not zero, the wavelength dependence of FR causes the low-frequency parts of a received radar chirp to be more strongly rotated than high-frequency parts. As a result, a single-polarized sensor configuration will receive—

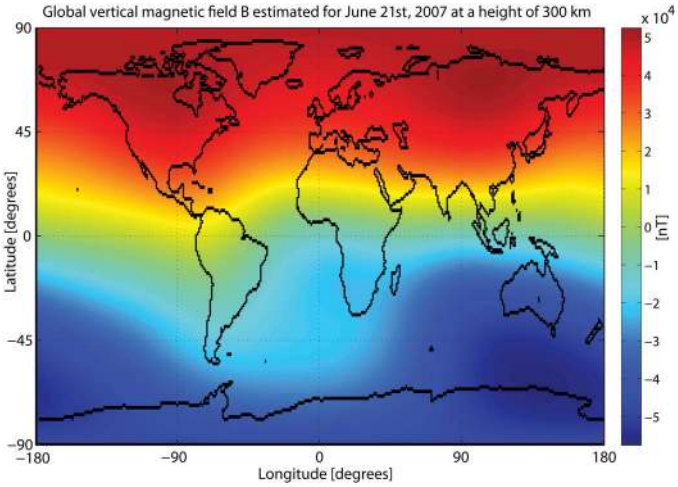

Fig. 1. Effective component of the geomagnetic field for a nadir-looking sensor. Magnetic field as modeled by the IGRF10 for June 21, 2007.

discernible for a point target—an apparently frequency-dependent change in amplitude of the transmitted chirp in the presence of FR.

Generally, FR depends on the total electron content and the magnetic field along the path and may be estimated from [5] and [7] as

$$\Omega = \frac{2.365\cdot 10^4}{c^2}\cdot\lambda^2\cdot B_{\parallel}\int_0^h N_e\,dh \approx \frac{2.365\cdot 10^4}{f^2}\cdot \mathrm{VTEC}\cdot\frac{1}{\cos\gamma}\cdot B_{\parallel} \quad (2)$$

where $B_{\parallel}$ is the mean parallel magnetic field in the line of sight of the sensor within the ionized layer, c is the speed of light, λ is the wavelength of the radar wave, VTEC is the vertical total electron content, and γ is the off-nadir angle of the observation. The factor $1/\cos\gamma$ converts the vertical electron content to the electron content along the ray path. The commonly used zenith angle of the radar wave at the subionospheric point was therefore approximated by the satellite's off-nadir angle. VTEC may be estimated using global ionospheric maps from the Center for Orbit Determination in Europe [22]. γ may be obtained for each image location in a product from the sensor data annotations for most currently active SAR satellites. Finally, the parallel magnetic field was obtained at a height of 300 km from the IGRF10 model presented in Section II-A. As the strength of geomagnetic field varies slowly at ionospheric heights, a reference mean value is commonly estimated for a set reference height between 300 and 450 km [7].

C. Chirp Signal Path Delay

According to Hanssen [23], electromagnetic waves propagating through the ionosphere are delayed by

$$\Delta t_{\mathrm{iono}} = \frac{K}{c}\cdot\frac{\mathrm{TEC}}{f_c^2} \quad (3)$$

where TEC is the total electron content along the signal path and $K = 40.28\ \mathrm{m^3/s^2}$ is a refractive constant. This means

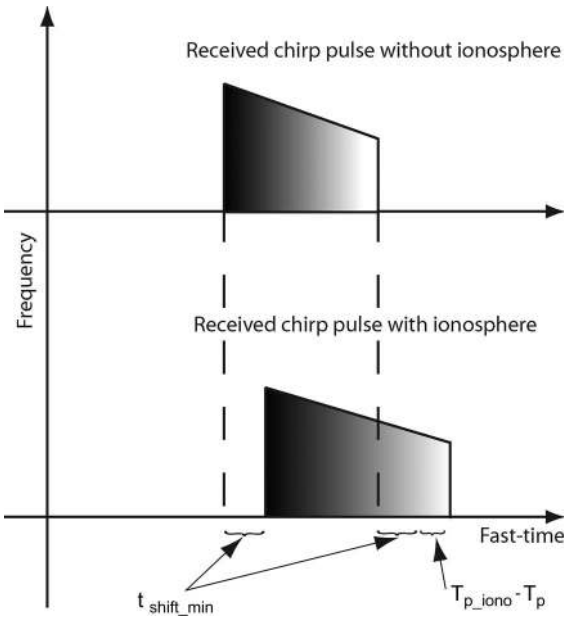

Fig. 2. (Top) Received chirp pulse without and (bottom) including ionospheric effects.

that for a down-chirp (e.g., PALSAR chirp) and a two-way propagation from satellite to Earth and back, the pulse is shifted between

$$t_{\text{shift\_min}} = \frac{2}{c}\, K \cdot \frac{\text{TEC}}{f_{\text{start}}^2} \tag{4}$$

$$t_{\text{shift\_max}} = \frac{2}{c}\, K \cdot \frac{\text{TEC}}{f_{\text{stop}}^2}. \tag{5}$$

For a linearly frequency-modulated chirp, these shifts imply a change in the chirp rate and, therefore, a change in the length of the transmitted pulse. In a precise simulation of TEC influence on SAR signals, this behavior of the ionosphere must be considered by including $t_{\text{shift\_min}}$ in the received signal. Because of the frequency-dependent path delays, given high ionospheric conditions, also a modified chirp rate replaces the transmitted chirp rate in the received pulse. Fig. 2 shows these effects including the shifts in range and the modified chirp rate. T_p is the pulse duration of the transmitted chirp, and T_{p_iono} is the new pulse duration of the chirp after passing the ionosphere (two-way). Because the phase refractive index of a radio wave in the ionosphere is less than unity, a two-way phase advance at center frequency f_c relative to that in free space may be estimated as

$$\phi_{\text{ph}} \approx \frac{2K}{cf_c^2} \cdot \text{TEC}. \tag{6}$$

Finally, the rate of change of phase with respect to frequency, also known as the phase dispersion $\phi_r(f)$, i.e., the residual phase function at frequency f caused by the nonturbulent ionosphere, may be modeled as [24]

$$\phi_r(f) \approx \frac{4\pi K}{cf_c^3} \cdot \text{TEC}(f - f_c)^2. \tag{7}$$

Local or traveling ionospheric disturbances (TIDs) that are difficult to foresee may also play a role [18]. Because of the limited spatial area affected, they influence the standard deviation of a scene measurement of TEC and FR but otherwise only pose a problem for pointwise applications like SAR interferometry [5].

TABLE I
SATELLITE SENSOR DETAILS AND ESTIMATES (TWO-WAY) OF INFLUENCE OF 50 AND 100 TECU ON THE PATH DELAY, CHIRP LENGTH, AND FR FOR TERRASAR-X (TS-X), ALOS PALSAR, AND A POSSIBLE FUTURE SPACEBORNE P-BAND SENSOR CONFIGURATION. THE EARTH'S MAGNETIC FIELD IS MODELED FOR JUNE 21, 2007, 45° NORTH AND 0° EAST, AT A HEIGHT OF 300 KM AND A NADIR-LOOKING SENSOR CONFIGURATION

Sensor	**TS-X**		**PALSAR**		**P-band**	
Frequency (f_c) [GHz]	9.65		1.27		0.45	
Bandwidth (B) [MHz]	max. 300		max. 28		6	
Chirp duration [μsec]	40*		27		27	
Sampling rate [MHz]	max. 330		max. 32		8	
Chirp form	up		down		down	
Orbit (altitude) [km]	514		695		695	
TEC [TECU]	50	100	50	100	50	100
Path delay at f_c [m]	0.5	1	27	54	218	436
Change in chirp length for B [$n$sec]	-0.1	-0.2	4	8	19.4	38.7
Faraday rotation at f_c [°]	0.5	1	29.5	59	235	470
Δ FR within chirp [°]	0.03	0.06	1.3	2.6	6.3	12.5
$\varnothing$ Amplitude variation (M_{hh}) [dB]	-44	-38	-8.9	-3.1	-2.0	-1.3
Δ Amplitude within chirp (M_{hh}) [dB]	-53	-47	-19.5	-14.1	-10.5	-6.9

*Chirp duration for TerraSAR-X estimated using typical conversion factors based on PRF.

In summary, signal FR and path delays caused by the ionosphere depend on the chirp bandwidth and increase at lower carrier frequencies. Table I shows the influence of the ionosphere at 50 and 100 TEC units ($1\ \text{TECU} = 1 \times 10^{16}\ \text{m}^{-2}$) based on calculations from the above theory for the TerraSAR X and ALOS PALSAR systems as well as a possible configuration of a P-band spaceborne sensor. For the calculations of amplitude variations, refer to Section III-C.

III. SIMULATIONS

Compared to TEC values *normally* found in the ionosphere, the numbers listed in Table I are quite high. However, these values highlight the phenomena they cause, particularly when the phenomena are subtle. Simulations made using a range of TEC values are presented in the following section together with the necessary detailed simulation background and process explanations.

A. Chirp Signal Path Delay

Under high ionospheric conditions, visible differences in the SAR raw data result mainly in a slant range (fast time) positional shift. Relevant changes appear when correlating the received pulses with a replica of the transmitted chirp in order to perform pulse compression—a matched filter operation, where best compression of the pulses is achieved when the transmitted and received pulses match perfectly. In the time domain, matched filtering of the pulse corresponds to a convolution of

the received chirp $s(t)$ with the complex conjugate $p^*(t)$ of the transmitted chirp, providing the desired compressed return echo

$$s_M(t) = s(t) \otimes p^*(t) \tag{8}$$
$$= \mathcal{F}^{-1}\left\{S(w) \cdot P^*(w)\right\} \tag{9}$$

where $\otimes$ denotes a convolution and * as the complex conjugate operator. By using this information and the theory presented in Section II-C, the duration of the received pulse may be estimated as

$$T_{p\_\text{iono}} = T_p \pm \frac{2}{c} \cdot K \cdot \text{TEC} \cdot \left(\frac{1}{(f_c - f_0)^2} - \frac{1}{(f_c + f_0)^2}\right) \tag{10}$$

depending (in contrast to the transmitted chirp) additionally on the TEC value. f_0 denotes the half chirp bandwidth. The corresponding chirp rate is

$$\alpha_{\text{iono}} = \frac{f_0}{T_{p\_\text{iono}}}. \tag{11}$$

The expected form of the received chirp under the influence of the ionosphere can be written as

$$s_{\text{iono}} = e^{j2\pi\left(f_{\text{start}} \cdot t_{d0} - \alpha_{\text{iono}} \cdot t_{d0}^2\right)} \tag{12}$$

where t_{d0} is a time vector depending on the sensor's sampling rate and the range to the target Y_c according to

$$t_{d0} = \frac{2Y_c}{c} + (0 : n-1) \cdot \frac{1}{f_s} + \Delta t_{d0} \tag{13}$$

$$\Delta t_{d0} = 2 \cdot (0 : n-1) \cdot \frac{K \cdot \text{TEC}}{(f_c \pm f_0)^2} \cdot c \tag{14}$$

where Δt_{d0} includes the frequency-dependent behavior of the chirp. The "$\pm$" is derived from the choice of down- versus up-chirp. n is an integer satisfying the condition

$$(n-1) \cdot \frac{1}{f_s} \leqslant T_{p\_\text{iono}}. \tag{15}$$

In the following simulations, the raw data were estimated using a standard system model proposed in [25, Ch. 6] with an antenna beam pattern dependent mainly on the center frequency and the physical antenna length. Without loss of generality, we assume that any antenna gain-dependent effects on the SAR signal have been corrected and removed from the SAR data. The standard system model has been extended to include all ionospheric effects discussed in Section II, including time and phase shifts of the chirp due to the nonturbulent ionosphere, but TID and nonequal antenna gains of different polarizations are left out of the simulation, as they would not add significant information. Azimuth compression was performed using the $\omega - k$ algorithm. For detailed information on the SAR focusing steps, the reader is referred to [25] and [26].

B. FR Simulation

All independent channels of a multipolarized SAR are affected by FR in the same way. Therefore, a single model for these effects is sufficient. An approach described in [13] is used here to retrieve the measured scattering matrix $\mathbf{M_0}$. It may be written as

$$\mathbf{M_0} = A e^{j\varphi} \mathbf{R}^{\mathrm{T}} \mathbf{R}_F \mathbf{S} \mathbf{R}_F \mathbf{T} + \mathbf{N} \tag{16}$$

where $\mathbf{S}$ is the scattering matrix, $\mathbf{R}$ and $\mathbf{T}$ are the receive and transmit distortion matrices, $\mathbf{N}$ is additive noise, A is the amplitude of the received pulse after the matched filter, $e^{j\varphi}$ is the signal phase, and $\mathbf{R}_F$ is the one-way FR matrix. As the focus here lies on FR, in the forgoing, the parameters $e^{j\varphi}$, A, $\mathbf{T}$, and $\mathbf{R}$ can be independently calibrated: Within the simulation, calibration errors are not modeled [12]. In our simulation, $\mathbf{N}$ varies from zero, for an ideal case, to -30 dB, corresponding to reasonable PALSAR noise equivalent sigma zero (NESZ) values for polarimetric mode [27]. Under ideal conditions, (16) simplifies to

$$\mathbf{M} = \mathbf{R}_F \mathbf{S} \mathbf{R}_F \tag{17}$$

or

$$\begin{bmatrix} M_{\text{hh}} & M_{\text{vh}} \\ M_{\text{hv}} & M_{\text{vv}} \end{bmatrix} = \begin{bmatrix} \cos\Omega & \sin\Omega \\ -\sin\Omega & \cos\Omega \end{bmatrix} \cdot \begin{bmatrix} S_{\text{hh}} & S_{\text{vh}} \\ S_{\text{hv}} & S_{\text{vv}} \end{bmatrix} \cdot \begin{bmatrix} \cos\Omega & \sin\Omega \\ -\sin\Omega & \cos\Omega \end{bmatrix}. \tag{18}$$

Under backscatter alignment conditions, (18) can be written as

$$\begin{aligned} M_{\text{hh}} &= S_{\text{hh}} \cos^2\Omega - S_{\text{vv}} \sin^2\Omega + (S_{\text{hv}} - S_{\text{vh}}) \sin\Omega \cos\Omega \\ M_{\text{vh}} &= S_{\text{vh}} \cos^2\Omega + S_{\text{hv}} \sin^2\Omega + (S_{\text{hh}} + S_{\text{vv}}) \sin\Omega \cos\Omega \\ M_{\text{hv}} &= S_{\text{hv}} \cos^2\Omega + S_{\text{vh}} \sin^2\Omega - (S_{\text{hh}} + S_{\text{vv}}) \sin\Omega \cos\Omega \\ M_{\text{vv}} &= S_{\text{vv}} \cos^2\Omega - S_{\text{hh}} \sin^2\Omega + (S_{\text{hv}} - S_{\text{vh}}) \sin\Omega \cos\Omega. \end{aligned} \tag{19}$$

In our simulation, we consider reflection symmetry, where we assume a constant signal return amplitude $B = S_{\text{hv}} = S_{\text{vh}}$. This reduces (19) to

$$\begin{aligned} M_{\text{hh}} &= S_{\text{hh}} \cos^2\Omega - S_{\text{vv}} \sin^2\Omega \\ M_{\text{vh}} &= B + (S_{\text{hh}} + S_{\text{vv}}) \cdot \sin\Omega \cos\Omega \\ M_{\text{hv}} &= B - (S_{\text{hh}} + S_{\text{vv}}) \cdot \sin\Omega \cos\Omega \\ M_{\text{vv}} &= S_{\text{vv}} \cos^2\Omega - S_{\text{hh}} \sin^2\Omega \end{aligned} \tag{20}$$

which in the case of a trihedral corner reflector (TCR). A point target with $A = S_{\text{hh}} = S_{\text{vv}}$ can be rewritten as

$$\begin{aligned} M_{\text{hh}} &= A \cdot \cos 2\Omega \\ M_{\text{vh}} &= B + A \cdot \sin 2\Omega \\ M_{\text{hv}} &= B - A \cdot \sin 2\Omega \\ M_{\text{vv}} &= A \cdot \cos 2\Omega. \end{aligned} \tag{21}$$

By using the aforementioned assumptions for calibration and TCR measurements, the backscatter behavior is implemented as described in (21) with noise added in the nonideal case. For simplicity, the amplitude A was set to one and B to zero, corresponding to the backscatter behavior of an ideal TCR.

C. Chirp Amplitude Variations Because of FR

The chirp amplitude variation caused by FR is also modeled in the simulation. The single-polarized amplitude is used to

model the received pulse subject to FR. For a single channel, e.g., HH, the received pulse is modeled with (12) and (21) as

$$s_{\mathrm{FR}} = M_{\mathrm{hh}} \cdot e^{j2\pi\left(f_{\mathrm{start}} \cdot t_{d0} - \alpha_{\mathrm{iono}} \cdot t_{d0}^2\right)}. \tag{22}$$

Because M_{hh} depends on the FR angle Ω, which, in turn, depends on the frequency f, a frequency-dependent amplitude variation is to be expected. At L-band—under the PALSAR system parameters and NESZ assumptions—the expected frequency-dependent change in amplitude might not be detectable at TEC levels below 15 TECU. The reason becomes clear if one thinks about the small change of FR angles within the typical 14-MHz range bandwidth of quad-polarized PALSAR data. An attenuation would, however, be clearly observable with a spaceborne P-band system. The results from Table I show that under higher ionospheric conditions and at lower frequencies, amplitude variations within a chirp can rise to above the noise level and degrade the image quality.

The change in FR $\Delta\Omega$ within the chirp bandwidth may be estimated from single-polarized data using (21)

$$\Omega_1 = \frac{1}{2}\arccos\left(\frac{M_{\mathrm{hh}_1}}{A}\right) \tag{23}$$

$$\Omega_2 = \frac{1}{2}\arccos\left(\frac{M_{\mathrm{hh}_2}}{A}\right) \tag{24}$$

$$\Delta\Omega = \Omega_1 - \Omega_2 \tag{25}$$

$$= \frac{1}{2}\left(\arccos\frac{M_{\mathrm{hh}_1}}{A} - \arccos\frac{M_{\mathrm{hh}_2}}{A}\right) \tag{26}$$

where M_{hh_1} and M_{hh_2} are the amplitudes of the chirp at its respective start and stop frequencies. Low sampling rates can distort the accuracy of the measurements of both amplitudes by misestimating the location of the maxima. Measurement of the *difference* of the amplitudes removes the necessity to estimate the absolute value of the amplitudes M_{hh_1} and M_{hh_2}. The relative difference in amplitude can be obtained from the mean gradient within the amplitudes and the chirp bandwidth. It is therefore probably more accurate to calculate $\Delta\Omega$ from the difference in amplitude $\Delta A = M_{\mathrm{hh}_1} - M_{\mathrm{hh}_2}$ within the chirp. Using a series expansion for the arccos function

$$\arccos x = \frac{\pi}{2} - \left[x + \frac{x^3}{2\cdot 3} + \frac{1\cdot 3x^5}{2\cdot 4\cdot 5} + \frac{1\cdot 3\cdot 5x^7}{2\cdot 4\cdot 6\cdot 7} + \cdots + \frac{1\cdot 3\cdot 5\cdots(2n-1)x^{2n+1}}{2\cdot 4\cdot 6\cdots(2n)(2n+1)} + \cdots\right] \quad \text{for all } |x| < 1 \in \mathbb{R} \tag{27}$$

and (26) as

$$2\Delta\Omega = \frac{\pi}{2} - \left[\frac{M_{\mathrm{hh}_1}}{A} + \frac{M_{\mathrm{hh}_1}^3}{6A^3} + \frac{3M_{\mathrm{hh}_1}^5}{40A^5} + \cdots\right] - \frac{\pi}{2} + \left[\frac{M_{\mathrm{hh}_2}}{A} + \frac{M_{\mathrm{hh}_2}^3}{6A^3} + \frac{3M_{\mathrm{hh}_2}^5}{40A^5} + \cdots\right] \quad \text{for all } \left|\frac{M_{\mathrm{hh}_1}}{A}\right|, \left|\frac{M_{\mathrm{hh}_2}}{A}\right| < 1 \in \mathbb{R}. \tag{28}$$

Neglecting terms of higher order reduces (28) to

$$\Delta\Omega \approx \frac{M_{\mathrm{hh}_2} - M_{\mathrm{hh}_1}}{2\cdot A} = \frac{-\Delta A}{2\cdot A}. \tag{29}$$

D. FR Extraction

There exist a number of methods for the extraction of FR from quad-polarized data. The most well known are given in [1] and [12]. The approach described in [1] is the most robust because it estimates FR using the phase between the cross-polarized (left/right) circular states. It was used throughout our investigations.

For simulated data, the algorithm presented in [12] would work as well and is easier to implement. It defines the two-way FR by observing that

$$\Omega_{2-\mathrm{way}} = 2\cdot\frac{1}{2}\arctan\left[\frac{(M_{\mathrm{vh}} - M_{\mathrm{hv}})}{(M_{\mathrm{hh}} + M_{\mathrm{vv}})}\right]. \tag{30}$$

Similarly, the circular cross-pol method [1] states that

$$\Omega_{2-\mathrm{way}} = 2\cdot\frac{1}{4}\arg\left(Z_{12}Z_{21}^*\right) \tag{31}$$

with

$$\begin{bmatrix} Z_{11} & Z_{12} \\ Z_{21} & Z_{22} \end{bmatrix} = \begin{bmatrix} 1 & j \\ j & 1 \end{bmatrix} \cdot \begin{bmatrix} M_{\mathrm{hh}} & M_{\mathrm{vh}} \\ M_{\mathrm{hv}} & M_{\mathrm{vv}} \end{bmatrix} \cdot \begin{bmatrix} 1 & j \\ j & 1 \end{bmatrix}.$$

The results from the method described in [1] can easily be analyzed using the simulation model developed earlier. To allow comparison with the results in Section IV, the PALSAR system parameters listed in Table I were used. However, simulations were done with 14-MHz bandwidth, as PALSAR does not support higher bandwidths in polarimetric mode [28]. Noise with a level of -30 dB was added to each channel. Simulations were conducted at 20 TECU, a reasonable value at average solar conditions. Equation (2) indicates that 20 TECU induce an FR angle of 11.812° at $f = f_c = 1.27$ GHz, and the Earth's magnetic field $B_\parallel$ is modeled at a height of 300 km for June 21, 2007, 45° North and 0° East. The peak of the focused point target in the simulation is at 20 dB.

Fig. 3 shows the results of an analysis of simulated raw data. In Fig. 3(a), the FR values over the complete scene are shown calculated with (31). Where a chirp signal is present, FR varies between 11.68° and 11.94°, as predicted in theoretical calculations. As this is only a single point target, the variations are due to the change of frequency *inside* the chirp, not to slant range or off-nadir angle variations (constant for a single stationary TCR on the ground). The influence of noise is very visible at the border of the chirp signal. The retrieved mean FR angle was $\Omega_\varnothing = 11.8132^\circ$ with a standard deviation of $\sigma_\Omega = 0.16774^\circ$ (no noise: $\sigma_\Omega = 0.07531^\circ$).

An almost uniform distribution of values is observed, caused by the characteristics of the chirp passing over a single TCR. An SNR threshold was applied in the figure, discarding values in Fig. 3(a) below a 5% limit of peak signal power. In the following, we compare compressed signals where the noise level of images increases due to the nonideal matched filtering. In Fig. 3(b) and (c), the range and azimuth profiles are plotted.

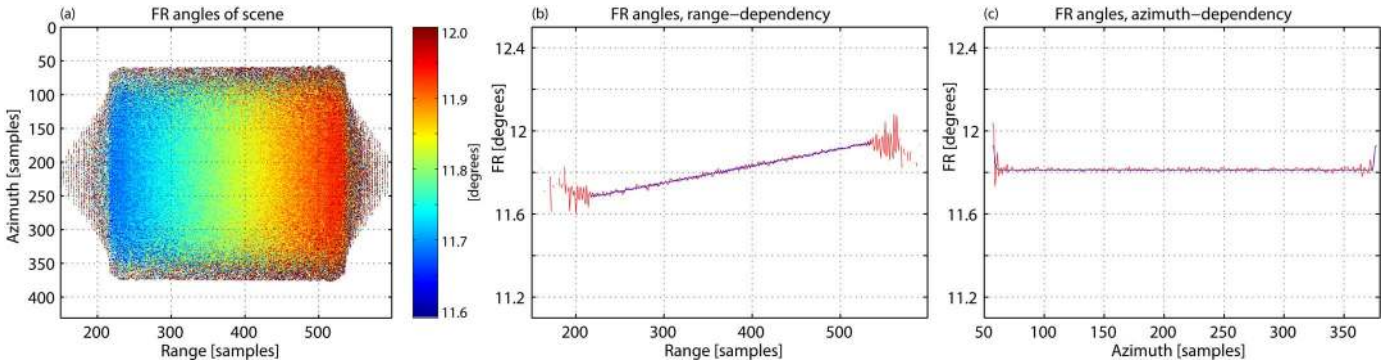

Fig. 3. FR analysis on *simulated* PALSAR **raw** data of a TCR at scene center for 20 TECU. In (a), the FR values of the received quad-polarized signal from the TCR are calculated with (31). FR varies between 11.68° and 11.94°. In (b) and (c), the mean range and azimuth profiles, respectively, are plotted. Blue: Without noise. Red: NESZ $= -30$ dB added.

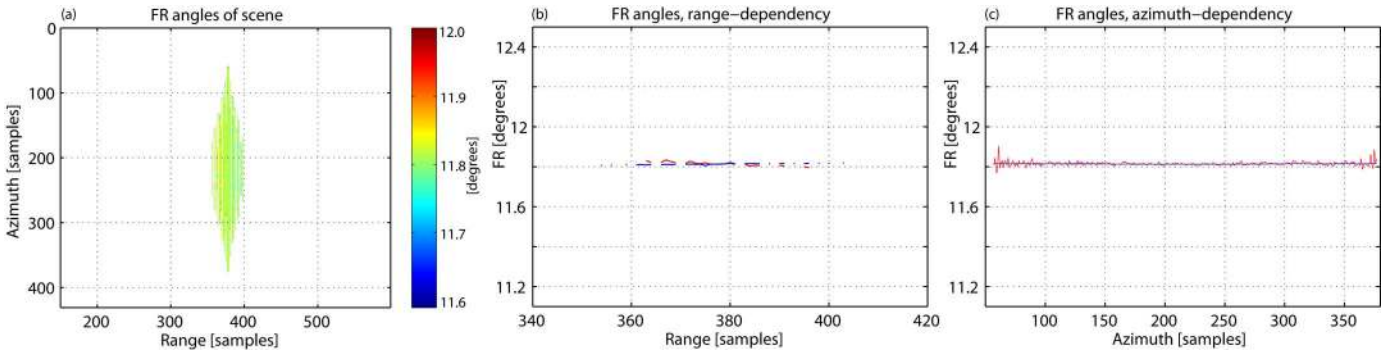

Fig. 4. FR analysis on *simulated* PALSAR RC data of a TCR at scene center for 20 TECU. In (a), the FR values of the quad-polarized and compressed signal are calculated with (31). Areas with no signal are masked out. In (b) and (c), the mean range and azimuth profiles, respectively, are plotted. Blue: Without noise. Red: NESZ $= -30$ dB added.

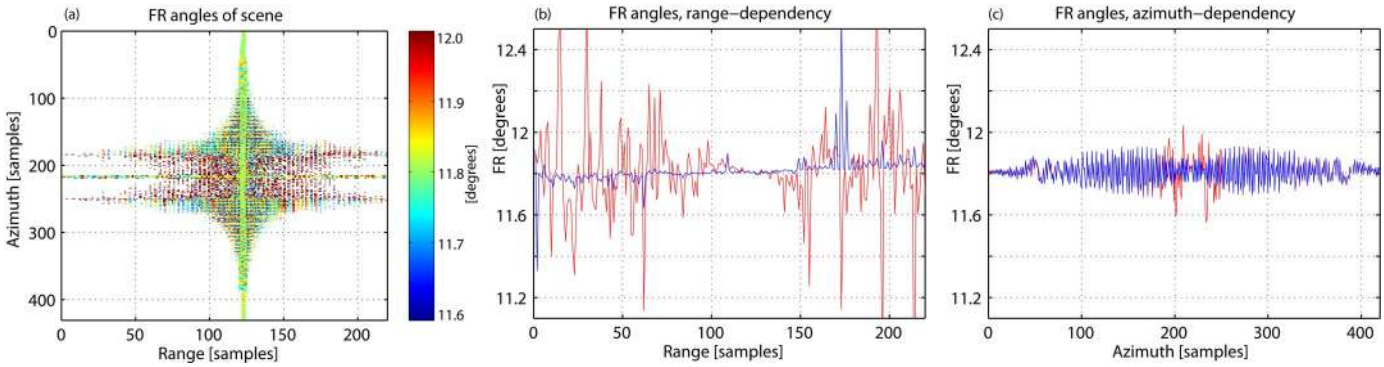

Fig. 5. FR analysis on *simulated* PALSAR AC data of a TCR at scene center for 20 TECU. In (a), the FR values of the quad-polarized and compressed signal are calculated with (31). Areas with no signal are masked out. The mean range and azimuth profiles are plotted in (b) and (c). Blue: Without noise. Red: NESZ $= -30$ dB added.

Some border effects are observable. The edge effect in Fig. 3(c) is caused by variations in the aperture length which is always slightly longer in far-than-in-near range. Values retrieved from simulations without added noise are plotted for comparison, indicated in blue.

Similar results from the RC data derived from the raw data in Fig. 3 are shown in Fig. 4. Due to the compression, the signal in Fig. 4(a) is much more compact, clearly showing the SAR-typical azimuth characteristics of a dwell-time smearing in azimuth, typically focused later in azimuth compression. Power thresholding was applied to improve the image's SNR. FR estimates are much closer to a single value in Fig. 4(a) than in Fig. 3(a). The mean value of FR measured from the noised data is $\Omega_\varnothing = 11.8145^\circ$ with a standard deviation of $\sigma_\Omega = 0.02348^\circ$. After range compression in Fig. 4(b), one sees that the range dependence is completely lost. The standard deviation without noise yields $\sigma_\Omega = 0.00327^\circ$. Azimuth dependence in Fig. 4(c) again shows constant characteristics.

The AC data of the same TCR as in Figs. 3 and 4 are shown in Fig. 5. As before, in Fig. 5(a), the FR values for the complete scene are shown with the same power threshold applied. Areas with very weak backscatter, which become visible after azimuth compression, are removed. Still, there remain large regions in the scene where a signal is present and where FR analysis

TABLE II
RESULTS OF TWO-WAY FR AND STANDARD DEVIATION FOR SIMULATED PALSAR RAW, RC, AND AC DATA UNDER IONOSPHERIC CONDITIONS OF 20, 50, AND 100 TECU. SIMULATION WAS DONE FOR 100 TCRS WITH RANDOM AMPLITUDES BETWEEN 0 AND 1 AND TWO NOISE LEVELS

	NESZ	-30 dB		-25 dB	
TEC	Data	∅FR[°]	σ_Ω[°]	∅FR[°]	σ_Ω[°]
20 [TECU]	RAW	11.83	0.07	11.83	0.09
	RC	11.87	0.06	11.87	0.07
	AC	11.87	0.18	11.87	0.33
50 [TECU]	RAW	29.56	0.18	29.56	0.18
	RC	29.68	0.12	29.68	0.13
	AC	29.66	0.31	29.66	0.42
100 [TECU]	RAW	59.13	0.35	59.13	0.35
	RC	59.35	0.27	59.35	0.27
	AC	59.30	0.87	59.30	0.91

may be applied. The results are consistent with those shown for the RC and raw data scene. However, as may be seen in Fig. 5(b), the simulations including noise produce retrievals that oscillate around the mean value (red line), whereas the ideal data give an almost constant value of FR over range (blue line). The calculated mean FR is $\Omega_\varnothing = 11.8091^\circ$ with a standard deviation of $\sigma_\Omega = 0.52256^\circ$ with noise ($\sigma_\Omega = 0.12383^\circ$ no noise). This is confirmed by the azimuth trend of a cut through the TCR that shows a constant value with a large standard deviation. The variation is reduced if a threshold is chosen that cuts off more of the signal. The signal of an AC simulated TCR has a high peak power value at its focal point and only low signals (sidelobes) around it.

For a more meaningful comparison with real data measurements, a set of 100 simulated TCRs was investigated under mean ionospheric conditions of 20, 50, and 100 TECU and for two different noise levels (-30 and -25 dB). TEC was therefore modeled to be range dependent. The amplitudes ($S_{\mathrm{hh}} = S_{\mathrm{vv}}$) of the TCRs were randomly set between zero and one. Table II shows extracted two-way FR values and related standard deviations. Fig. 6 shows an example of the histograms of the extracted FR angles under mean ionospheric conditions of 20 TECU and a noise level of -25 dB. The histogram shows the results in Fig. 6(a)–(c) for the raw, RC, and AC data, respectively. The mean extracted FR angles from the data are (a) $\Omega_\varnothing = 11.826^\circ$, (b) $\Omega_\varnothing = 11.874^\circ$, and (c) $\Omega_\varnothing = 11.87^\circ$. The standard deviations are estimated to be (a) $\sigma_\Omega = 0.089^\circ$, 0.066°, and 0.332°, respectively.

Compared to the single TCR simulations, the spread of FR in the RC data is again lowest, but differences between the raw and RC become smaller. The spread of FR retrievals is highest for the fully focused data. Moreover, the mean value of the focused data is slightly increased in comparison to the raw data. The differences in extracted FR between the raw and focused data are again due to the nonideal focusing operations caused mainly by the frequency-dependent modifications of the chirp under ionospheric conditions. FR estimation from simulations at higher TEC levels increases correspondingly (see Table II). The influence of noise on the variation in FR angles is most relevant at lower TEC levels.

In P-band simulations, stronger FR dependence in range on the raw data is expected to be observed because of the larger relative change of frequencies inside the bandwidth relative to the center frequency.

IV. ALOS PALSAR DATA

After reviewing theoretical considerations with simulations, the step from simulations to real data measurements is a natural goal. With PALSAR, the first spaceborne system is operational where FR can significantly influence polarimetric measurements. The challenges of measuring FR from real data are a correct calibration of the polarimetric channels as well as background clutter, speckle, and the systematic noise sources.

A. Calibration and Validation

PALSAR was specifically designed to be a polarimetric SAR system. Its engineers therefore took great care to ensure that the antenna gain pattern could be consistently calibrated across all channels with the help of PALSAR antenna gain files [28]. Assuming stationarity, polarimetric calibration with preservation of the FR can be achieved by applying calibration parameters estimated within a scene known to have very low expected FR. The parameters can be estimated via the aforementioned algorithms or taken directly from Japan Aerospace Exploration Agency (JAXA) level 1.1 single look complex products. The integration of polarimetric calibration in the FR estimation based on SAR data was made using standard reference values from JAXA. The FR estimates were averaged over a rectangular area (according to projected range and azimuth resolutions).

For the estimation of the FR from the Global Navigation Satellite System (GNSS) TEC maps, the magnetic field was simulated at the scene center using the IGRF10 model for a height of 300 km. FR angles in the slant direction were estimated using the nadir component of the magnetic field and the vertical TEC over the scene center mapped by the satellite's off-nadir angle. Bihourly TEC maps sampled every 2.5° in latitude and 5.0° in longitude were interpolated to 1° resolution and temporally to the corresponding sense time between two consecutive TEC maps. The accuracy of the TEC maps over regions with high GPS receiver density (e.g., Europe) is advertised to be in the range of $\pm$3–4 TECU [29].

B. FR Measurement

Examining a set of 15 fully polarimetric ALOS PALSAR scenes from -10° to 50° latitude, expected two-way FR from the simulations ranges from 0.82° to 14.2°. Fig. 7 shows the two-way FR measurements from a data set where higher FR was expected from the TEC maps and the IGRF10 model. Values that are below a 5% limit of peak signal power and are over a 95% limit of peak signal power were masked out (marked in dark blue). The colorbar for FR over the scene in Fig. 7(a) is also valid for the scenes in Fig. 7(c), (e), and (g). Fig. 7(b), (d), and (f) shows normalized histograms corresponding to the FR scene on their left. Fig. 7(g) shows the FR angles of the azimuth focused scene with values below an 80% limit of peak signal power masked out. Fig. 7(h) compares the amplitudes of the focused image. The behavior of these results is generally

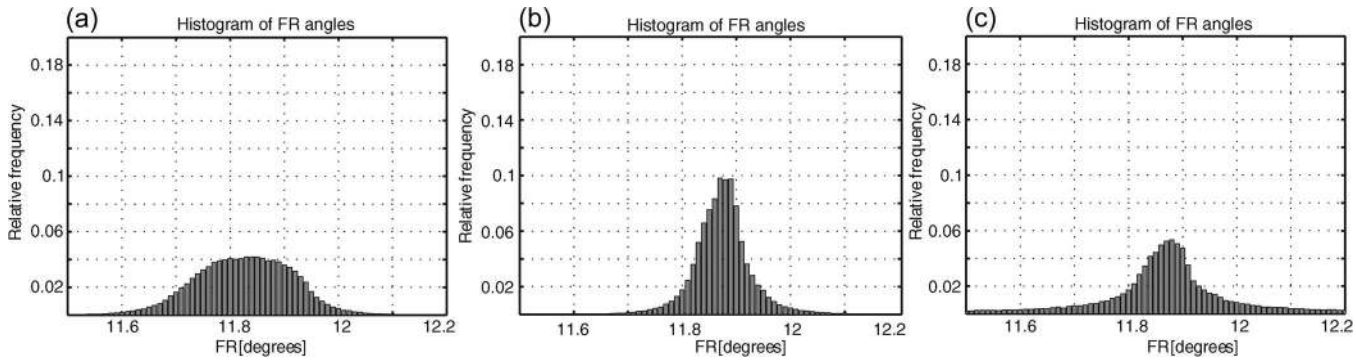

Fig. 6. Comparison of FR histograms from *simulated* PALSAR data of 100 TCRs at a mean TEC level of 20 TECU and −25-dB NESZ. (a) FR values from the *raw* data. (b) FR values from the RC data. (c) FR values from the AC data.

representative for all examined PALSAR scenes. Comparing the FR estimations from the raw [Fig. 7(a) and (b)], RC [Fig. 7(c) and (d)], and AC [Fig. 7(e) and (f)] data with the simulations, the same trends can be observed. FR from the raw data is closer to the trend of the simulations than the FR from the RC and AC data, as the raw data better fit the simulations than the focused data. The FR from the RC data is, as in the simulations, usually higher than the FR from the AC data. The broadness of the distribution of the real data increases with every compression step. From the simulations, we were able to observe this trend only with regard to the AC data. Standard deviations of raw and RC data from simulations of 100 TCRs became nearly identical.

Fig. 7(e) shows that areas where FR is undefined (colored in dark blue) or highly variable are typically dark regions such as lakes and mountainous backslope areas. No range and azimuth profiles are shown in Fig. 7, as in a large and complex scene; they only emphasize the variations and do not otherwise provide any useful information (assuming that ionospheric variations within the SAR image can be neglected). At L-band frequencies, given the observed variations, it is not feasible to extract any range-dependent FR from the range profile for the available data sets. For the raw data, not even the frequency dependence of FR within the chirp in a range profile can be shown (as analog to Fig. 3), as all frequencies overlap at every point in space. Therefore, the extracted FR angles from the raw data are influenced by the FR of all contributing scatterers within that pixel and are dominated by the strongest ones. As the FR variations of the scatterers are caused by the range and chirp bandwidth dependence, no significant spread of the standard deviation is expected. However, the presence of noise in the data increases the standard deviation and also causes a bias away from the "true" FR toward zero. However, as the SNR of the raw data is nearly constant throughout the data matrix, the FR variations are expected to stay small. The bias results in an underestimation of the FR when based on the raw data. The presence of multiple strong scatterers in a SAR scene reduces this bias, as they improve the SNR. After focusing the image, the standard deviation increases, as the SNR is now very inhomogeneous. While the accuracy decreases, the lowered bias improves the precision, as the SNR is largely higher than in the raw data.

To validate the presented FR measurement method not just for a single data set, data from multiple quad-polarized PALSAR scenes from -10° to 50° latitude at diverse ionospheric activity levels were examined. In Fig. 8, the results for 15 scenes are presented. The table to the right of Fig. 8 shows, in addition to the two-way FR angles, the standard deviation and the estimated/measured TEC levels from the simulation (TECU slant), and the TEC levels (TECU from AC) derived from the mean FR of the azimuth focused data using again the magnetic field over the scene center.

FR estimation for these scenes shows that the FR angles derived from GNSS-based simulations largely agree with the estimations from the real data, generally following the same trend. Very low estimations of FR at comparably high TEC levels (i.e., data set 1) are typically seen near the equator, where the parallel component of the magnetic field is small. The lower half of estimated FR from the real data tends to be *less* than the estimations from simulation. This behavior changes for higher FR and compressed data, where the frequency-dependent amplitude variations are generally above the NESZ level. FR from the raw data is usually lower than the estimates from the simulations, but its trend agrees more strongly with GNSS-based simulations. This was also observed in the TCR simulations in Section III-D. The standard deviation, as expected from Section IV-B, increases transitioning from the raw to the focused data. Estimated FR largely decreases from the RC to the AC data.

V. Discussion of Results

The simulation results show that raw data clearly are susceptible to the chirp frequency dependence: A good estimate of mean FR was achieved. Derivation of FR from raw data produces an average FR from all contributing frequencies and is dominated by its strongest scatterers. Also caused by the nearly constant SNR, FR variations are expected to stay small. The comparably low SNR in the raw data results in a noise-induced shift of FR angles toward zero, explaining why FR from the raw data tends to be underestimated. Equations (2) and (20) show that FR depends on wavelength. We therefore expect, in addition to a change in the chirp length, a variation in the amplitude of the varying frequency components of a chirp. Under strong ionospheric conditions, these frequency-dependent modifications of the chirp reduce the performance of the matched filter. FR retrievals from raw and RC signals will thus tend to be dominated by the frequency parts of the chirp with higher

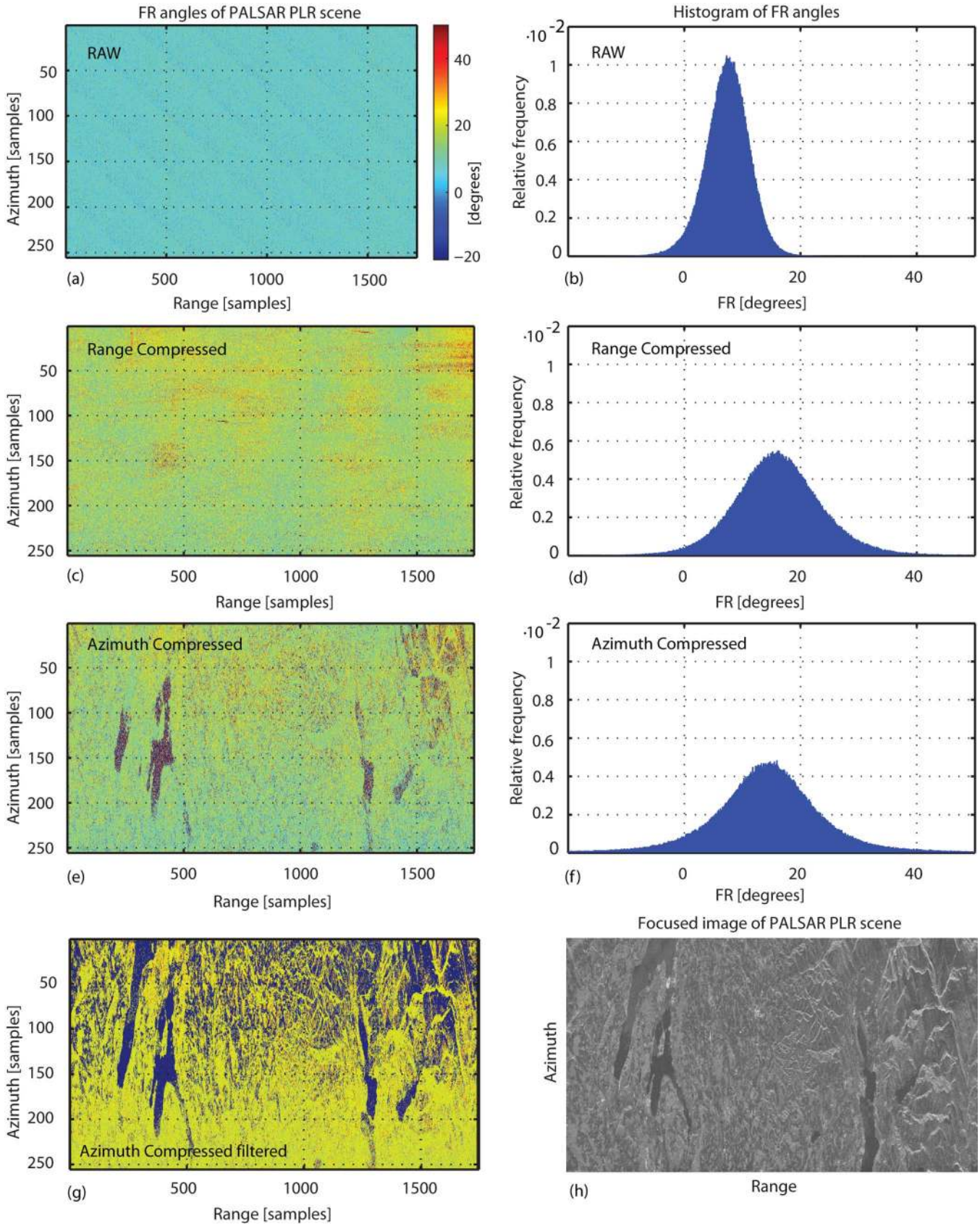

Fig. 7. (a) FR measurement from the PALSAR raw data. (b) FR histogram. (c) FR from RC data. (d) FR histogram for RC. (e) FR from AC data. (f) FR histogram for AC. In each case, the left image shows FR angles estimated for *individual* pixels of a scene, while the right image shows a histogram of the FR values. In (g), scatterers that are below an 80% limit of peak signal power of the AC data are masked out. (h) shows the corresponding HH amplitude image of the scene as a reference, allowing comparison of the AC FR measurements to the backscatter brightness and hence SNR level.

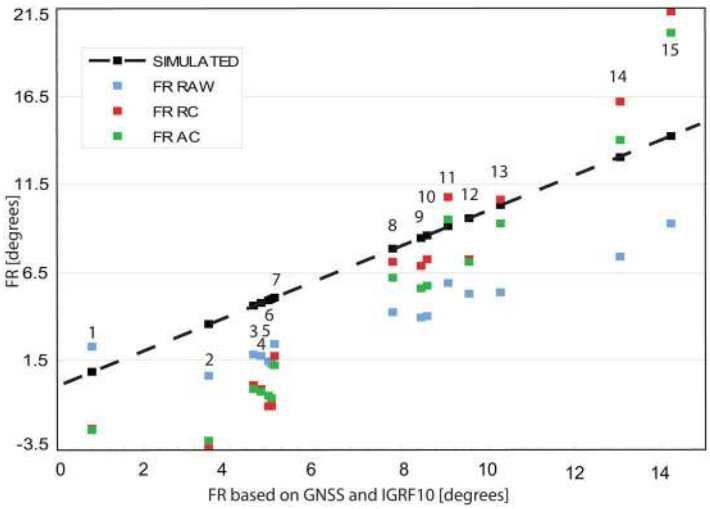

Data No.	Sim. FR	FR RAW	Std.dev. RAW	FR RC	Std.dev. RC	FR AC	Std.dev. AC	TECU slant	TECU from AC
1	0.8°	2.3°	3.5°	-2.4°	9.8°	-2.4°	8.0°	19.8	58.0
2	3.5°	0.7°	3.5°	-3.5°	9.0°	-3.1°	12.6°	5.7	5.0
3	4.6°	1.8°	3.4°	0.1°	8.8°	-0.1°	11.9°	7.4	0.2
4	4.8°	1.8°	3.5°	-0.2°	9.0°	-0.3°	13.2°	7.7	0.5
5	4.9°	1.4°	3.2°	-1.1°	11.2°	-0.5°	20.1°	8.0	0.8
6	5.0°	1.3°	3.3°	-1.1°	10.5°	-0.6°	18.8°	8.1	1.0
7	5.1°	2.4°	3.5°	1.8°	9.1°	1.2°	13.2°	8.1	1.9
8	7.8°	4.3°	3.6°	7.1°	8.7°	6.2°	11.3°	12.4	9.8
9	8.5°	3.9°	3.6°	6.8°	8.4°	5.6°	12.9°	13.6	9.0
10	8.6°	4.0°	3.7°	7.2°	8.9°	5.8°	14.0°	13.8	9.3
11	9.1°	5.9°	2.9°	10.8°	8.4°	9.5°	13.3°	14.6	15.3
12	9.6°	5.3°	4.4°	7.3°	21.8°	7.1°	19.7°	15.7	11.7
13	10.3°	5.3°	3.7°	10.6°	8.5°	9.3°	11.1°	16.3	14.8
14	13.0°	7.4°	3.7°	16.2°	7.7°	14.0°	13.0°	21.0	22.5
15	14.2°	9.3°	4.1°	21.3°	8.9°	20.1°	10.1°	23.8	33.6

Fig. 8. FR measurements from raw and focused PALSAR scenes from $-10°$ to $50°$ latitude at diverse ionospheric activity levels. For comparison, GNSS estimates from TEC maps were calculated for each scene (Sim. FR) and plotted as reference data (black line). The table lists the FR estimates and their standard deviation. TEC estimated from the AC data (TECU from AC) is also shown for comparison.

amplitudes. FR from AC signals shows improved robustness if thresholding is applied. The decision of whether raw, RC, or fully compressed images should be used for FR analysis depends on how well compression is able to focus individual targets and also on how high a power threshold value is applied. Higher thresholds yield better estimates and lower FR variations for a single TCR, but they also decrease the number of measurements available in a scene. High TEC levels increase the amplitude variations (within the range of ambiguity) within the chirp and can therefore reduce the reliability of the FR measurement.

The same considerations also apply for real data measurements. For real data, FR measurements of raw data tend to underestimate the true ionospheric TEC and FR effects. Tests where low-power signals were filtered out with a threshold showed the same effects as simulated data: inaccuracies in mean FR values and high FR variance caused by low SNR. Good examples of typical areas with low SNR are quiet water surfaces and mountainous backslopes [Fig. 7(e)]. As compression gives all targets an equal opportunity to express their individual FR, an important step toward improving the accuracy of measurements in focused data is therefore the masking out of low SNR regions. A uniform distribution of the FR as in the simulation of the raw data of a single point target cannot be achieved under real conditions.

Observations of trends for FR estimation over many real data scenes show that the FR angles derived from GNSS-based simulations follow the same trend as the estimations from raw and focused data. FR estimates from the raw data generally agree better with simulations, but there are larger differences at higher FR compared to results based on products. FR from the focused data with slant TEC levels below 12 TECU (estimations from TEC maps and the IGRF10 model) is generally around or below retrievals from the raw data.

The Bickel–Bates method [1] proves to be robust and shows that extracting FR from real quad-polarized PALSAR data provides comparable results to GNSS-derived FR. We were able to develop a screening tool that enables users of SAR data to scan a large catalog of PALSAR acquisitions for expected FR using only the sensor and acquisition details.

VI. Conclusion

Frequency-dependent propagation effects are a result of the influence of the ionosphere's electron content along the ray path and the Earth's magnetic field. In order to demonstrate the behavior of radar waves under different ionospheric conditions, a standard SAR simulation was implemented and extended to include ionospheric effects. Point target examples were used to simulate range shifts and frequency-dependent amplitude variations within a SAR image. An evaluation of a set of sensor configurations at P-, L- and X-bands showed that the influence of the ionosphere can become significant at lower frequencies. All polarimetric measurements are affected and must be corrected. Seen in a positive light, it could also enable the extraction of ionospheric FR and the generation of high-resolution TEC maps.

FR angle estimation using quad-polarized data was applied to simulated and real PALSAR data. It showed that the FR measurement approach discussed in [1] works well for raw, RC, and AC SAR data. In the simulations, the dependence of FR on the instantaneous frequency was seen, and a comparison between the measurements extracted from raw, RC, and AC data was made. The PALSAR data showed first results of FR angles as they appear in any operational polarimetric SAR system. FR retrievals based on GNSS measurements and the IGRF10 model agreed with extracted angles from raw and focused PALSAR data. The use of raw data for FR estimation is recommended, as the results agree better with retrievals from TEC maps and the simulated magnetic field than those based on the focused data. FR estimates from the raw data also generally have lower variability and are not subject to the nonideal focusing algorithms. However, underestimation of FR angles caused by the low SNR must be considered. SAR scenes over low reflecting areas are expected to be more strongly affected.

FR from focused data appears to be shifted due to the frequency-dependent amplitude variations and the change in chirp length that reduce the performance of the matched filter.

Calculation of FR using measured TEC maps, a magnetic field model, and the sensor annotations enables users of quad-polarized data to make first estimates of the FR in an acquired scene. No detailed scene-specific analysis of the SAR data is required. To validate the results from a single closely discussed example, data from multiple quad-polarized PALSAR scenes between -10° and 50° latitude at diverse ionospheric activity levels were examined.

Further investigations of the presented approaches, examining more data sets would enable delimitation of the estimation accuracy. It should not be forgotten that the simulations represent ideal situations. The 20 TECU used in the simulations treat the ionosphere at an average activity level. TEC values at these levels can be observed within PALSAR orbits at the programmed acquisition times even during the (presently occurring) solar minimum. The real data could be verified by GNSS. Making use of a polarimetric SAR offers much more than a single FR value: It can provide FR and TEC over a complete scene and at high resolution.

ACKNOWLEDGMENT

The authors would like to thank P. Pasquali of SARMap S.A. and B. Rosich of ESA-ESRIN for generously providing a large number of ALOS PALSAR raw data sets and also B. Rommen and B. Rastburg-Arbesser of ESA-ESTEC for their scientific input and financial support. The authors would also like to thank the anonymous reviewers for helping improve the quality of this paper.

REFERENCES

[1] S. H. Bickel and R. H. T. Bates, "Effects of magneto-ionic propagation on the polarization scattering matrix," *Proc. IEEE*, vol. 53, no. 8, pp. 1089–1091, Aug. 1965.

[2] M. Jehle, M. Rüegg, D. Small, E. Meier, and D. Nüesch, "Estimation of ionospheric TEC and Faraday rotation for L-band SAR," *Proc. SPIE*, vol. 5979, pp. 252–260, Oct. 2005.

[3] M. Jehle, M. Rüegg, D. Small, and E. Meier, "SAR data for TEC and Faraday rotation," Remote Sens. Labs., Univ. Zurich, Zurich, Switzerland, Final Rep. 20046/06/NL/CO, May 2007.

[4] F. Meyer, R. Bamler, N. Jakowski, and T. Fritz, "The potential of low-frequency SAR systems for mapping ionospheric TEC distributions," *IEEE Geosci. Remote Sens. Lett.*, vol. 3, no. 4, pp. 560–564, Oct. 2006.

[5] E. J. M. Rignot, "Effect of Faraday rotation on L-band interferometric and polarimetric synthetic-aperture radar data," *IEEE Trans. Geosci. Remote Sens.*, vol. 38, no. 1, pp. 383–390, Jan. 2000.

[6] W. B. Gail, "Effect of Faraday rotation on polarimetric SAR," *IEEE Trans. Aerosp. Electron. Syst.*, vol. 34, no. 1, pp. 301–307, Jan. 1998.

[7] P. A. Wright, S. Quegan, N. S. Wheadon, and C. D. Hall, "Faraday rotation effects on L-band spaceborne data," *IEEE Trans. Geosci. Remote Sens.*, vol. 41, no. 12, pp. 2735–2744, Dec. 2003.

[8] R.-Y. Qi and Y.-Q. Jin, "Analysis of the effects of Faraday rotation on spaceborne polarimetric SAR observations at P-band," *IEEE Trans. Geosci. Remote Sens.*, vol. 45, no. 5, pp. 1115–1122, May 2007.

[9] J. Liu, Y. Kuga, A. Ishimaru, X. Pi, and A. Freeman, "Ionospheric effects on SAR imaging: A numerical study," *IEEE Trans. Geosci. Remote Sens.*, vol. 41, no. 5, pp. 939–947, May 2003.

[10] D. M. L. Vine, S. D. Jacob, E. P. Dinnat, P. de Matthaeis, and S. Abraham, "The influence of antenna pattern on Faraday rotation in remote sensing at P-band," *IEEE Trans. Geosci. Remote Sens.*, vol. 45, no. 9, pp. 2737–2746, Sep. 2007.

[11] A. Freeman and S. S. Saatchi, "On the detection of Faraday rotation in linearly polarized L-band SAR backscatter signatures," *IEEE Trans. Geosci. Remote Sens.*, vol. 42, no. 8, pp. 1607–1616, Aug. 2004.

[12] A. Freeman, "Calibration of linearly polarized polarimetric SAR data subject to Faraday rotation," *IEEE Trans. Geosci. Remote Sens.*, vol. 42, no. 8, pp. 1617–1624, Aug. 2004.

[13] W. B. Gail, "A simplified calibration technique for polarimetric radars," in *Proc. IGARSS*, Tokyo, Japan, Aug. 1993, vol. 2, pp. 377–379.

[14] R. Touzi and M. Shimada, "On the use of symmetric scatterers for calibration and validation of PALSAR polarimetric modes," in *Proc. IGARSS*, Anchorage, AK, Sep. 2004, vol. 3, pp. 1835–1837.

[15] D. H. Hoekman and M. J. Quiriones, "Land cover type and biomass classification using AirSAR data for evaluation of monitoring scenarios in the Colombian Amazon," *IEEE Trans. Geosci. Remote Sens.*, vol. 38, no. 2, pp. 685–696, Mar. 2000.

[16] B. Hallberg, G. Smith, A. Olofsson, and L. M. H. Ulander, "Performance simulation of spaceborne P-band SAR for global biomass retrieval," in *Proc. IGARSS*, Anchorage, AK, Sep. 2004, vol. 1, pp. 503–506.

[17] J. Nicoll, F. Meyer, and M. Jehle, "Prediction and detection of Faraday rotation in ALOS PALSAR data," in *Proc. IGARSS*, Barcelona, Spain, Jul. 2007, pp. 5210–5213.

[18] Z.-W. Xu, J. Wu, and Z.-S. Wu, "A survey of ionospheric effects on space-based radar," *Waves Random Media*, vol. 14, no. 12, pp. 189–272, Apr. 2004.

[19] S. Macmillan and S. Maus, "International geomagnetic reference field—The tenth generation," *Earth Planets Space*, vol. 57, no. 12, pp. 1135–1140, Dec. 2005.

[20] R. A. Langel, *The Main Field*, vol. 1. New York: Academic, 1987.

[21] S. Chapman and J. Bartels, *Geomagnetism*. London, U.K.: Oxford Univ. Press, 1940.

[22] U. Hugentobler, M. Meindl, G. Beutler, H. Bock, R. Dach, A. Jäggi, C. Urschl, L. Mervart, M. Rothacher, S. Schaer, E. Brockmann, D. Ineichen, A. Wiget, U. Wild, G. Weber, H. Habrich, and C. Boucher, "CODE IGS analysis center Technical Report 2003/2004," Astron. Inst., Univ. Bern, Bern, Switzerland, 2004. Annual Tech. Rep. [Online]. Available: http://www.aiub.unibe.ch/content/research/gnss/publications/

[23] R. F. Hanssen, *Radar Interferometry*, vol. 2. Norwell, MA: Kluwer, 2001, ch. 6.3 Ionospheric Influences.

[24] K. Davies and E. K. Smith, "Ionospheric effects on satellite land mobile systems," *IEEE Antennas Propag. Mag.*, vol. 44, no. 6, pp. 24–31, Dec. 2002.

[25] M. Soumekh, *Synthetic Aperture Radar Signal Processing With MATLAB Algorithms*. New York: Wiley, 1999.

[26] I. G. Cumming and F. H. Wong, *Digital Processing of Synthetic Aperture Radar Data, Algorithms and Implementation*. Boston, MA: Artech House, 2005.

[27] M. Shimada, A. Rosenqvist, M. Watanabe, and T. Tadono, "The polarimetric and interferometric potential of ALOS PALSAR," in *Proc. POLinSAR*, Frascati, Italy, Jan. 2005.

[28] *Information on ALOS PALSAR Products for ADEN Users*, Apr. 2007, European Space Agency. Technical Note ALOS-GSEG-EOPG-TN-07-0001.

[29] M. Sekido, T. Kondo, E. Kawai, and M. Imae, "Evaluation of GPS-based ionospheric TEC map by comparing with VLBI data," *Radio Sci.*, vol. 38, no. 4, pp. 8-1–8-22, Jul. 2003.

Michael Jehle (S'07) received the Dipl.-Ing. degree in electrical engineering from the University of Karlsruhe, Karlsruhe, Germany, in spring 2002. He has been working toward the Ph.D. degree at the University of Zürich, Zürich, Switzerland, since the end of 2003.

After that, he worked as a Scientist in projects with the Institute for Very High Frequency Technology and Electronics, University of Karlsruhe, and with the Klinikum für Sportorthopädie Abteilung Biomechanik, Albert–Ludwigs University, Freiburg, Germany. He is currently a Research Assistant with the Remote Sensing Laboratories, University of Zürich. His research interests include electromagnetic wave propagation in the atmosphere, signal processing, and SAR systems.

Maurice Rüegg (S'00–M'07) received the M.Sc. degree in electrical engineering from the Swiss Federal Institute of Technology, ETH Zürich, Switzerland, in 2003 and the Ph.D. degree in microwave remote sensing from the Remote Sensing Laboratories, University of Zürich, Zürich, Switzerland, in 2007.

He is currently a Software Engineer for the foreign exchange and money markets business of UBS Investment Bank, Opfikon, Switzerland. His research interests included detection techniques for ground moving targets in SAR, SAR focusing algorithms, data simulations, and millimeter-wave radar. Upon completion of his dissertation, his broader computer science interests led him to a private industry.

Lukas Zuberbühler received the M.Sc. degree in geography from the University of Zürich, Zürich, Switzerland, in 2006, where he has been working toward the Ph.D. degree since the end of 2006.

He is currently a Research Assistant with the Remote Sensing Laboratories, University of Zürich. His research interests include modeling of polarimetric SAR data, forest parameter retrieval from polarimetric SAR, and bistatic polarimetric SAR.

David Small (S'85–M'98) received the B.A.Sc. degree in systems design engineering from the University of Waterloo, Waterloo, ON, Canada, in 1988, the M.A.Sc. degree in electrical engineering from the University of British Columbia, Vancouver, BC, Canada, in 1991, and the Ph.D. degree from the Remote Sensing Laboratories, Department of Geography, University of Zürich, Zürich, Switzerland, in 1998.

He has worked in the fields of SAR polarimetry and interferometry, as well as the geometric and radiometric calibration of SAR imagery. In his Ph.D. thesis, he developed a processing chain for generating digital elevation models from repeat-pass ERS data. He has worked on the geometric calibration of the ENVISAT ASAR sensor as a member of the quality working group. He is currently a Research Scientist with the Remote Sensing Laboratories.

Erich Meier received the M.Sc. degree in geography and the Ph.D. (Hons.) degree in remote sensing from the University of Zürich, Zürich, Switzerland, in 1982 and 1989, respectively.

From 1979 to 1982, he was a Research Assistant with the Remote Sensing Section, and from 1982 to 1983, he was with the GIS Laboratory, Department of Geography, University of Zürich. From 1983 to 2006, he was a Research Scientist with the Remote Sensing Laboratories (RSL), University of Zürich, where he is currently a Research Section Head who is involved in teaching as well as in research in digital image processing, software development for computer graphics, and radiometric and geometric calibration of SAR and optical imagery. Since 2000, he has been the Head of the SARLab, a research group within RSL. His main research interests of this group include the development of new focusing algorithms for SAR data from UHF to millimeter wave, interferometry, polarimetry, and MTI algorithms as well as calibration and validation activities for spaceborne and airborne systems. He is responsible for the research strategies as well as the organization of the team. He is a Consultant on behalf of several national and international organizations and private companies.